



## Ghost plumes hidden beneath Earth's continents

Simone Pilia <sup>a</sup> , Giampiero Iaffaldano <sup>b</sup> , D. Rhodri Davies <sup>c</sup>, Mohammad Ismaiel <sup>d</sup> , Paolo A. Sossi <sup>e</sup>, Scott Whattam <sup>a</sup>, Dapeng Zhao <sup>f</sup>, Hao Hu <sup>g,h,\*</sup>

<sup>a</sup> College of Petroleum Engineering and Geosciences, King Fahd University of Petroleum and Minerals, Dhahran, Saudi Arabia

<sup>b</sup> Department of Chemistry, Life Sciences and Environmental Sustainability, University of Parma, Parma, Italy

<sup>c</sup> Research School of Earth Sciences, Australian National University, Canberra, Australia

<sup>d</sup> Department of Earth and Climate Sciences, Indian Institute of Science Education and Research-Pune, Maharashtra, India

<sup>e</sup> Institute of Geochemistry and Petrology, ETH Zürich, Zürich, Switzerland

<sup>f</sup> Department of Geophysics, Graduate School of Science, Tohoku University, Sendai, Japan

<sup>g</sup> Advanced Research Institute of Applied Geology and Geophysics, Zhejiang University of Water Resources and Electric Power, Hangzhou, China

<sup>h</sup> College of Civil Engineering and Architecture, Zhejiang University of Water Resources and Electric Power, Hangzhou, China

### ARTICLE INFO

Editor: Dr C Carolina Lithgow-Bertelloni

**Keywords:**

Mantle plumes

Indian plate

Seismic tomography

Plate tectonics

Mantle

Oman

### ABSTRACT

Mantle plumes are hot, buoyant upwellings that rise from Earth's core-mantle-boundary (CMB) at ~2890 km depth to the surface. As they ascend towards the lithosphere – our planet's rigid outermost shell – decompression melting results in surface volcanism. In continental interiors, a thicker lithosphere restricts plume ascent and associated decompression melting. However, it remains uncertain whether limited continental volcanism implies few sub-continental mantle plumes. Here, we present inter-disciplinary evidence revealing the first clear example of an amagmatic “ghost” plume in eastern Oman – the Dani plume. Despite lacking present-day surface volcanism, this plume is robustly imaged using P- and S-wave arrival-time residuals from distant earthquakes, recorded by a dense regional seismic network. A positive thermal anomaly is further corroborated by a ~14 depression of the 410-km discontinuity and a ~20 km upward deflection of the 660-km discontinuity. The imaged low-velocity structure is overlain by positive present-day residual topography in a region enigmatically uplifted since the late Eocene (~40 Ma). Our analyses of kinematic reconstructions demonstrate that asthenospheric flow associated with the Dani plume modified Indian-plate motion in the late Eocene, allowing us to bound the likely arrival time of this plume beneath the lithosphere. Besides offering an approach to identify hidden continental plumes, both at the present-day and via Earth's geological record, our study suggests that CMB heat-flux estimates should be revised upwards, with implications for thermal and core evolution models.

### 1. Introduction

Mantle plumes are responsible for many of the volcanic tracks that extend across Earth's surface (Morgan, 1971; Davies et al., 2015). They play a fundamental role in the evolution of our planet through: i) the interplay between mantle convection, plate tectonics and surface processes (Morgan, 1971); ii) the initiation of seafloor spreading and early Earth subduction (Hill, 1991; Gerya et al., 2015); iii) global mass extinction events (Sobolev et al., 2011); and iv) the genesis of large nickel, platinum and diamond deposits (Torsvik et al., 2010). There are few known instances where such plumes currently rise from Earth's core-mantle boundary (CMB) at ~2890 km and intersect with continents. A recent study (Koppers et al., 2021) compiled a catalogue of deep

mantle plumes, reaching full consensus on the existence of only one continental plume (Afar) out of a potential twelve, and thus underscoring the difficulty of unequivocally identifying sub-continental plumes. In the oceanic realm, out of forty-five proposals, consensus has been reached for seven plumes. Nonetheless, given that plumes generate magmatism through decompression melting, such differences may be expected: plume-related volcanism should generally be more prevalent above thinner oceanic lithosphere (Steinberger and Becker, 2018) (average thickness ~75 km but age dependent), at locations such as Hawaii (French and Romanowicz, 2015), Reunion (Dongmo Wamba et al., 2023), and Iceland (Wolfe et al., 1997), than on the continents, where average lithospheric thicknesses are greater (on average 200 km with variations depending on the tectonic regime). But are plumes less

\* Corresponding author.

E-mail address: [huhao@zjwu.edu.cn](mailto:huhao@zjwu.edu.cn) (H. Hu).

common beneath continents, or are they “hidden”? Intraplate volcanism has traditionally served as the principal marker for identifying mantle plumes (Morgan, 1971; Courtillot et al., 2003). However, challenges arise in continental regions where complex structure and thick lithosphere inhibit decompression melting and the transport of any molten material to the surface. Typically, when surface volcanism is absent or

old, mantle-plume proposals have been rejected, or merely dismissed as “fossil plumes” (Witte et al., 2017; Stein and Hofmann, 1992).

In this paper we detect a “ghost” plume in eastern Oman, where, despite no obvious present-day volcanic activity, its presence is identified based upon seismic tomography images, mapping of thermally induced changes in thickness across the mantle transition zone, and

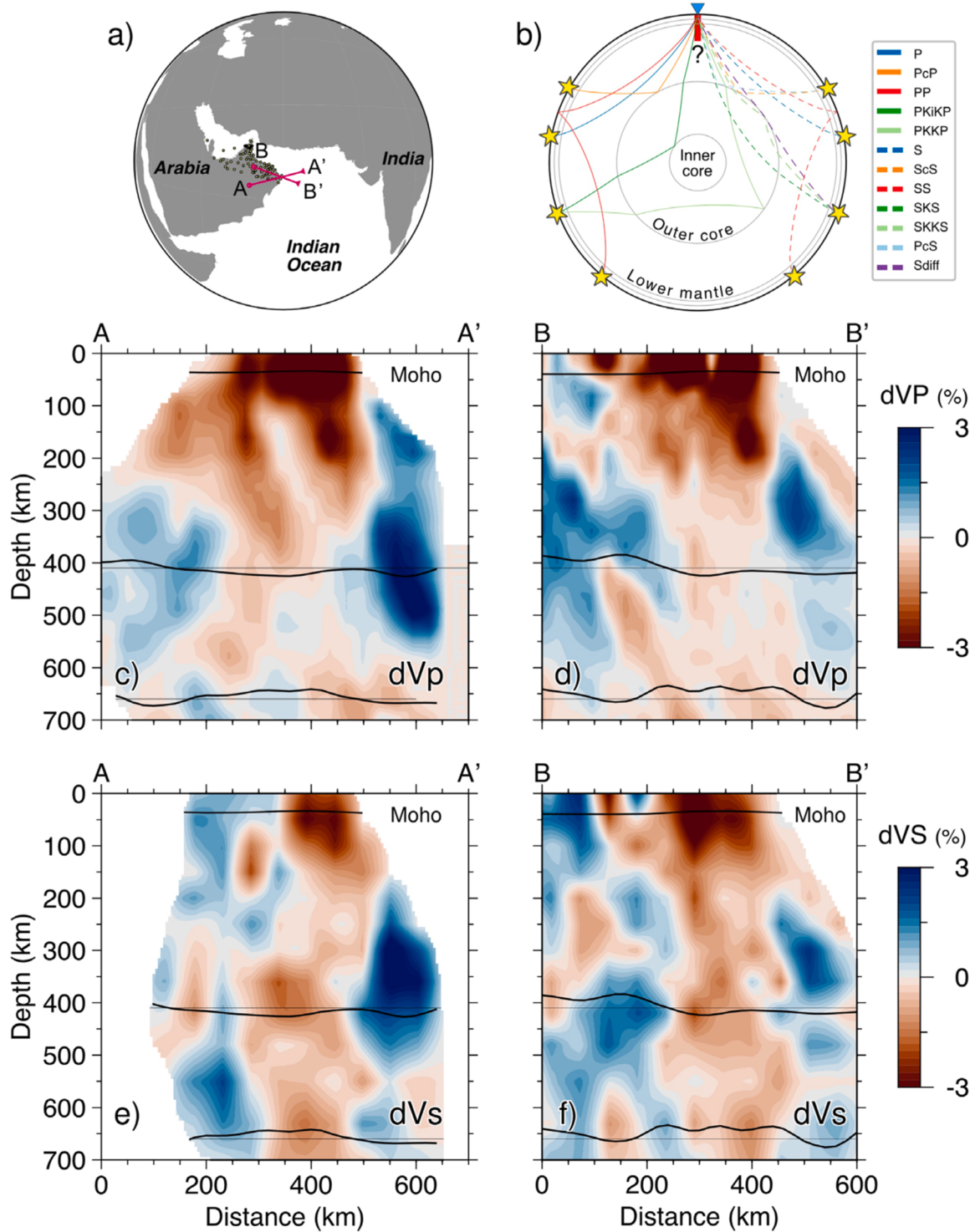


**Fig. 1. Tomographic images of the Dani plume.** a) Geographic distribution of seismic stations (dots) employed for tomographic inversion, along with purple lines delineating location of cross-sections through final P- and S-wave tomographic models. b) Illustration of teleseismic phases used for tomographic inversion. Stars denote hypothetical teleseismic hypocentres, and the blue inverted triangle marks the seismic network location, beneath which a conceptualized plume is positioned (in red). (c, d) Vertical profiles extracted from the P-wave tomographic model; (e, f) Corresponding profiles from the S-wave tomographic model. Black lines outline the d410 and d660 mantle discontinuities obtained in this study.

geological evidence for past and ongoing dynamic uplift. Constraints from plate kinematics indicate that this plume, which was located adjacent to the Indian plate at  $\sim 40$  Ma, is responsible for the azimuthal change recorded in the Indian plate motion at this time. Our study implies that the identification of continental mantle plumes based primarily on the observation of past/present volcanic activity is a false dichotomy.

## 2. Data and methods

### 2.1. Seismic data

Teleseismic waveforms are sourced from a network of 115 seismic broadband stations (30 permanent, 85 temporary) in the United Arab Emirates (UAE)-Oman region (Figs 1a and S1). The permanent stations are maintained by the national seismic networks of the UAE and Oman. The data from Oman consist primarily of 47 temporary stations of the COOL experiment (Weidle et al., 2013), deployed between January 2013 to December 2016. The remaining 38 temporary stations were deployed in the UAE by the former Petroleum Institute from June 2014 to December 2016 (Pilia et al., 2020a).

### 2.2. Seismic tomography

Multi-phase P and S waveforms were targeted and extracted from the continuous raw datasets using the criteria highlighted in Table 1. Waveforms were cut from -100 to 100 s around the predicted arrival times of the ak135 reference model (Kennett et al., 1995). Subsequent to removing the linear trend and instrument response, we applied a bandpass filter (with corner frequencies of 0.1 and 2.0 Hz) to each seismogram. We then calculated the signal-to-noise ratio (SNR) of each seismogram (Pilia et al., 2020b; Hu et al., 2023). Only traces with SNR greater than 1.5 were retained for subsequent processing steps. We extracted P-phases from the vertical-component seismograms, while S-related phases are measured from rotated horizontal-component seismograms, with the corresponding travel-time residuals determined based on waveform quality on either component (see Table 1). The majority of arrivals originate from the first-arriving P- or S-waves travelling in the mantle at angles between  $\sim 25^\circ$  and  $\sim 45^\circ$  to the vertical under each station. Including core phases travelling within  $\sim 20^\circ$  to the vertical under each station enables ample ray-crossing (Fig. 1b), enhancing tomography accuracy.

The arrival travel-time residuals are computed using an adaptive stacking approach (Rawlinson and Kennet, 2004), as performed in Pilia et al. (2023). Our dataset for tomographic inversion eventually consists

**Table 1**

The selection criteria and number of events of each seismic phase used in this study.

Phase name	P-related phases				
	P	PcP	PKKP	PKiKP	PP
Distance ( $^\circ$ )	27-98	27-60	35-120	27-150	27-180
No. events	487	1	3	85	83
Component	Z	Z	Z	Z	Z
No. residuals	19022	20	62	3288	2064
Phase name	S-related phases				
	PcS	S	ScS	Sdiff	SKKS
Distance ( $^\circ$ )	27-	27-	27-	95-	105-
	65	98	60	145	145
No. events	5	134	25	12	16
Component	R	T	T	T	R
No. residuals	73	1772	321	154	167
					243
					35

\*Noting that all the events have  $M_b \geq 5.0$

of 24,456 P-related wave travel-time residuals from 659 events, and 2,765 S-related wave travel-time residuals from 219 events (Table 1).

A crustal correction was made to reduce the effect of crustal heterogeneities on teleseismic travel-time residuals. To this end, S-wave velocities from surface-wave tomography (Pilia et al., 2020a; Weidle et al., 2022) were used to create a 3-D crustal model. For the P-wave tomographic model, S-wave velocities were converted to P velocities using the relationship of Brocher (2005). The correction for an event-station pair is estimated using the following equation:

$$\delta t_{crust} = t_{3D} - t_{ak135} \quad (1)$$

where  $t_{3D}$  represents the crustal travel time for a given event-station pair calculated for the 3-D crustal velocity model described earlier;  $t_{ak135}$  is the crustal travel-time computed for 1-D crustal velocities of the ak135 reference model (Kennett et al., 1995);  $\delta t_{crust}$  indicates the difference resulting from the 3-D inhomogeneous crust. Thus, the corrected relative arrival-time residual is represented by:

$$t_{cc} = t_{res} - \delta t_{crust} \quad (2)$$

where  $t_{cc}$  and  $t_{res}$  indicate the relative travel-time residuals after and before the crustal correction, respectively.

The tomographic method includes a 3-D ray tracing routine and the LSQR approach subject to smoothing and damping regularizations (Zhao et al., 1994). We conducted two independent inversions for 3-D P- and S-wave velocity (Vp, Vs) models down to 1000 km depth. The 3-D model is parameterized by a horizontal grid interval of  $0.3^\circ$  and  $0.5^\circ$  for the Vp and Vs models, respectively. The vertical grid interval for the Vp model is 20 km at depths of 0-200 km, followed by 30 km interval at depths of 200-700 km, and finally every 100 km interval down to the model bottom at 1000 km depth. That is different for the Vs model, where initially the vertical grid interval is 50 km, which then increases to 80 km at 550 km depth, and finally every 100 km down to the model bottom at 1000 km depth. After the parameterization, the 3-D Vp and Vs models contain 28,413 and 6,175 grid nodes, respectively. Depth variations of the Moho discontinuity from receiver functions (Weidle et al., 2022; Ismaiel et al., 2023) are incorporated in the 3-D ray tracing and tomographic inversions. To evaluate the opportune trade-off among the data variance, model variance and model roughness, a so-called L-curve (or trade-off curve) approach is used to determine the optimal damping and smoothing parameters required for inversions (Zhao et al., 1994).

### 2.3. 410-km and 660-km seismic discontinuities

We use the seismic records from 49 temporary broadband stations deployed under the COOL project for 3-D Common Conversion Point (CCP) imaging. The seismic waveforms for receiver-function analysis are from  $Mw > 5.5$  earthquakes with epicentral distance between  $30^\circ - 90^\circ$ . Waveforms are detrended and filtered by applying a Butterworth filter from 0.05 to 2 Hz. The horizontal components are rotated into radial and transverse (RT) components based on back-azimuth angle. The waveforms are then trimmed around theoretical P arrival time (10 s before and 120 s after the arrival time). The theoretical P arrival time was calculated using the ak135 velocity model. Seismic records with low SNR ratio ( $< 3$ ) are rejected and remaining records were used for calculating the P-wave RFs using iteration time-domain deconvolution method (Gauss factor = 2, number of iterations = 400) (Ligorria and Ammon, 1999). The PRFs data were converted to depth using a crust-corrected (Pilia et al., 2020a; Weidle et al., 2022) ak135 velocity model. The Ps-P time difference and locations of pierce points were generated at an interval of 1 km in vertical depth from 300 to 800 km and 2-D horizontal grid bins were designed with a lateral interval of  $0.5^\circ$  and circle shape of bin with radius of 75 km. All the PRFs were stacked with pierce points falling in each bin and 95% confidence intervals were calculated using bootstrap method. Both 410-km and 660-km discontinuities (d410 and d660, respectively) were calculated using the Seispy

package (Xu and He, 2023).

### 3. Results

#### 3.1. A mantle plume in eastern Oman

Inversion of arrival-time residuals from teleseismic earthquake data (Fig. 1b and Fig. S1) provide P- and S-wave speed variations in the lithosphere and underlying upper-mantle. Our 3-D P- and S-wave tomographic analyses consistently image a sub-vertical low-velocity anomaly, originating below 660 km depth and extending into the uppermost mantle beneath eastern Oman (Fig. 1c-f and Fig. S2). This anomaly has a diameter of 200–300 km (synthetic experiment in Figs 2 and S3), vertical continuity, and quasi-cylindrical geometry. Based on this observation, along with additional evidence presented in the following sections, we infer the presence of a newly identified mantle plume, which we call the Dani plume. Northeastern Oman has experienced subduction of Neo-Tethys oceanic crust in the Late Cretaceous and underthrusting of the Arabian continental margin beneath the Semail ophiolite, so a steep, high-velocity core interpreted as a slab relict is enclosed on three sides by the broader low-velocity conduit of the Dani plume (e.g., Fig. S2 at 100 km depth, coordinates 23°N–57°E). Other isolated high-velocity pixels that punctuate the low-velocity column fall below the resolution threshold and fluctuate with minor changes in regularization; they are therefore treated as artefacts, whereas the conduit itself is robust to regularization parameter choices. A 3-D view of the Dani plume is provided in Supplementary Fig. S4.

Upper-mantle seismic velocities are strongly sensitive to temperature: a 100 °C increase in temperature would typically result in a decrease of 0.5–2% for Vp and 0.7–4.5% for Vs (Goes et al., 2000; Stixrude and Lithgow-Bertelloni, 2012), highlighting the greater temperature sensitivity of S-waves. Assuming a Vs derivative with respect to temperature of 1% per 100 °C, the estimated peak excess temperature of the Dani plume relative to ambient upper mantle, given maximum Vs anomalies of -3% up to 200 km beneath the surface (Fig. 1), is therefore ~100–300 °C, acknowledging the potential amplitude reduction due to regularization in the inversion process, wavefront healing, and diminishing anelastic contributions with increasing depth below 200–300 km (Goes et al., 2004; Styles et al., 2011). The 100–300°C bracket is deliberately conservative: restoring the 20–30 % amplitude damping would enlarge the velocity anomaly, whereas choosing the lower end of published Vs–temperature derivatives would likewise push the excess temperature toward the upper bound.

To assess our ability to recover the vertical and lateral extent of the low-velocity anomaly presented in Fig. 1, we performed a series of resolution tests employing synthetic structures. Synthetic arrival-time residuals are generated using an identical source-receiver combination and phase types as the observed dataset. Rays are traced through a known low-velocity structure, simulating a plume with a peak velocity perturbation of 3% (Figs 2 and S3). This synthetic plume is designed with a 200 km diameter vertical conduit and a head with a thickness of 150 km and a diameter of 350 km. It is important to note that, due to variations in node interval in the Vp and Vs models, the synthetic plume is not exactly the same in both models. Following this, Gaussian noise with standard deviations of 0.1 and 0.2 s is introduced to all synthetic P and S travel-time residuals, respectively, to simulate the picking errors observed in the real data. The recovered models (Figs 2, S3 and S5) suggest that the vertical low-velocity anomaly we image beneath eastern Oman is laterally well resolved and can be faithfully recovered with both P and S residual times if present in the observational dataset. However, our test shows that the Vs anomalies are significantly underestimated (approximately by 30%) below ~150 km depth (a known limitation of regularization).

The presence of thermal anomalies at depth can also be inferred from the topography of the d410 and d660 seismic discontinuities, which are sensitive to temperature variations owing to the opposing signs of the

Clapeyron slopes associated with their respective phase transitions (e.g., Katsura and Ito, 1989; Ito and Takahashi, 1989). These discontinuities correspond to solid-state phase transitions in the olivine component of mantle rocks. We analyzed the conversion of P- to S-waves using the receiver function technique to image mantle transition zone discontinuities, and then superimposed these results onto our tomographic profiles (Fig. 1c-f). The d410 discontinuity shows a depression of ~14 km, primarily confined to the region of relatively low velocity that defines the Dani plume. In contrast, the d660 discontinuity appears deflected upwards by ~20 km in correspondence of the low-velocity anomaly imaged tomographically.

#### 3.2. Absence of current surface volcanism

The Dani plume does not generate present-day volcanism. While this has clearly hindered identification of the plume beneath eastern Oman, the lack of volcanism is not entirely unexpected, given the regional geological setting. Mantle plumes produce magmatism through decompression melting, at temperatures that exceed those of ambient mantle. The lithosphere, which acts as a lid to limit plume ascent and the minimum melting pressure (Humphreys and Niu, 2009), is estimated to be greater than 100 km thick above the Dani plume (Davies et al., 2019).

At corresponding pressures (3–4 GPa), even a plume with a modest excess temperature of ~150–250 °C (potential temperatures of ~1500–1600 °C), as estimated from imaged seismic velocities, would produce only limited melt, owing to the shallow  $dP/dT$  slope of the mantle peridotite solidus beyond these pressures (Hirschmann, 2000). In addition, as discussed further in the following sections, any plume's volcanic record prior to ~7 Ma has likely been lost due to the long-lived and ongoing subduction associated with closure of the Tethys Ocean (Müller et al., 2019). Limited present-day volcanism, and limited preservation of older volcanism, is therefore to be expected.

Before discussing the Dani plume, we first revisit the Batain basanites (Fig. S1) because, despite erupting close to the modern conduit of the Dani plume, their chemistry and palaeo-position tie them to Afar. High-resolution whole-rock  $^{40}\text{Ar}/^{39}\text{Ar}$  age determination of these basanites reveals virtually continuous Late Eocene magmatic activity from ~40.7 to ~35.3 Ma (Witte et al., 2017; Nasir et al., 2006). The Batain basanites have low SiO<sub>2</sub> contents that are indicative of partial melt extraction at high pressures (e.g., Walter & Cottrell, 2024). At pressures above ~2 GPa, Plank & Forsyth (2016) propose a correction to the pressures and temperatures derived from the thermobarometer of Lee et al. (2009) to account for the cryoscopic effect of CO<sub>2</sub> dissolution into the silicate liquid. Using their correction, mean source region temperatures of 1432 ± 31°C and pressures of 3.4 ± 0.2 GPa (90–135 km depth) are obtained, assuming loss-on-ignition values are representative of their initial H<sub>2</sub>O contents (Fig. 3a). These estimates are nevertheless higher than those reported by Witte et al. (2017) on the same samples ( $P \sim 2$ –2.5 GPa;  $T \sim 1250$ –1300°C) using the original thermobarometer of Lee et al. (2009), even though the CO<sub>2</sub> correction applied here shifts  $P$ - $T$  downwards. The discrepancy is likely related to the fact that in Witte et al. (2017) there is no correction for whole rock compositions, which are in equilibrium with olivine with forsterite contents between 85–89 (Fo<sub>85–89</sub>), to that typical of asthenospheric mantle, Fo<sub>90</sub>, as performed here, leading to anomalously low  $P$ - $T$  estimates.

Heavy rare-earth element (REE) depletion relative to Light REE (Witte et al., 2017) also attests to the presence of garnet in their source region and, hence, melting below the spinel-garnet phase transition, consistent with predictions of the thermobarometer. To constrain the chemical nature of the source region, we parameterise the shape of the chondrite-normalized REE abundances plotted against ionic radius by nth-order orthogonal polynomials (whose coefficients are denoted by  $\lambda_n$  (O'Neill, 2016)). Compared to oceanic basalts, the Batain basanites have  $\lambda_1$  (slope, 17.8 ± 1.0) and  $\lambda_2$  (curvature, 18 ± 8), occupying a region distinct from OIBs, which cluster around  $\lambda_1 = 14 \pm 5$  and  $\lambda_2 = -5 \pm 15$ . The degree of total rare earth element enrichment in the Batain

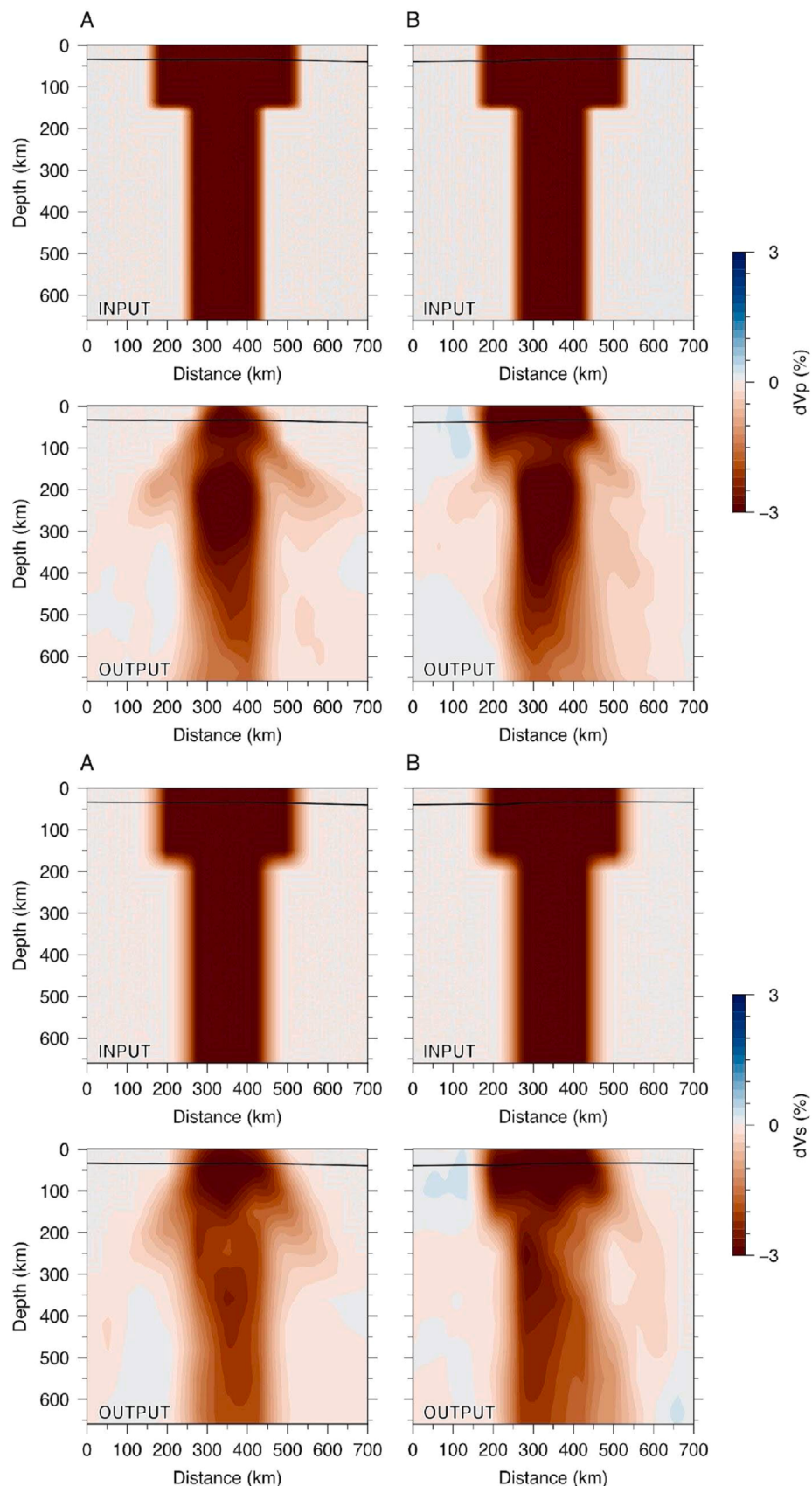


**Fig. 2. Resolution test for plume structure.** The resolution test assesses a synthetic plume structure featuring a low-velocity conduit with a 100 km radius and a 150 km thick and wider head. The upper and lower panels represent  $V_p$  and  $V_s$  structure, respectively. Input and output structures are labelled in the lower-left corner of each profile. Locations of profiles A and B are displayed in Fig. S3. Positive and negative velocity perturbations outside the target structure (both in the input and output profiles) are largely a function of the random Gaussian noise that is added to the synthetic data.

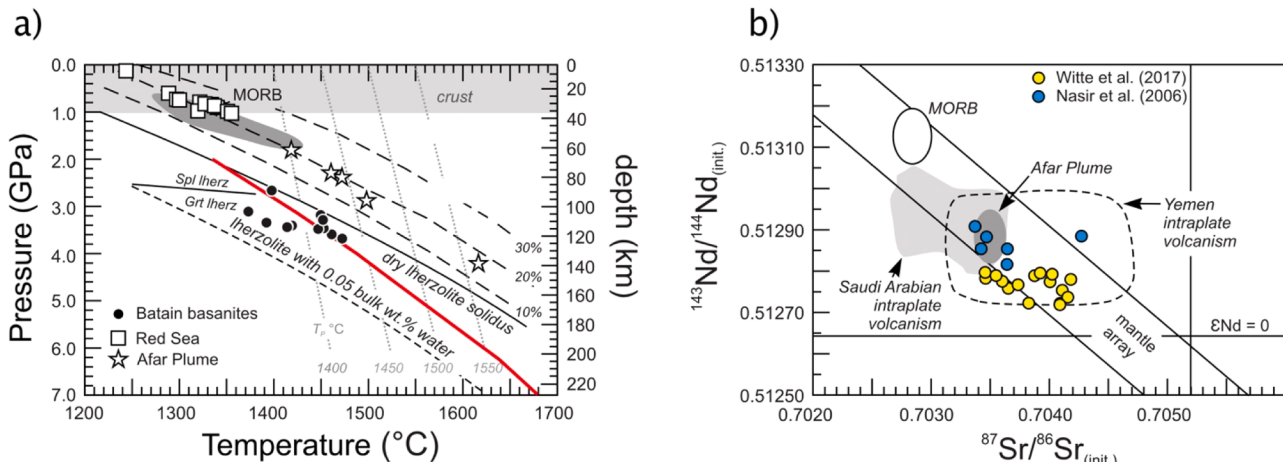


**Fig. 3. Potential temperatures, pressures and isotopes for Batain basanites.** Potential temperatures and pressures of sources of primitive lava and dike samples with  $\text{MgO} > 8 \text{ wt\%}$  and  $\text{Mg\#} > 60$  for Batain basanites (circles). Temperature and pressure calculated using Lee et al. (2009), and residual mantle compositions of  $\text{Fo}_{90}$  and  $\text{Fe}^{3+}/\sum\text{Fe}$  ratios of 0.10. It is also assumed the loss-on-ignition values represent  $\text{H}_2\text{O}$  and performing a temperature-pressure correction for the amount of  $\text{H}_2\text{O}$ , as well as for  $\text{CO}_2$  in the melt inferred from  $\text{SiO}_2$  contents following Plank & Forsyth (2016). Dry Iherzolite solidus (solid black line) and melt fraction isopleths (long dash black lines) are from Katz et al. (2003). Carbonated peridotite solidus in red from Dasgupta and Hirschmann (2010), included to show the  $\text{CO}_2$ -depressed melting temperatures appropriate for the basanites  $\text{CO}_2$ -rich source. Adiabats for mantle potential temperatures of 1400, 1450, 1500 and 1550°C are shown for reference as dashed lines. b) Initial  $^{143}\text{Nd}/^{144}\text{Nd}$  vs. initial  $^{87}\text{Sr}/^{86}\text{Sr}$  of Batain basanites (yellow circles from Witte et al. (2017)) and Muscat basanites (blue circles from Nasir et al. (2006)) vs. MORB, Afar Plume derived volcanics, Arabian basalts, and Yemen basalts (Baker et al., 1997). The Sr-Nd-Pb isotope systematics of the Batain basanites share affinities with the Afar plume, namely  $^{87}\text{Sr}/^{86}\text{Sr} \sim 0.704$ ,  $^{143}\text{Nd}/^{144}\text{Nd} \sim 0.5129$ ,  $^{206}\text{Pb}/^{204}\text{Pb} \sim 18.8$  and  $^{207}\text{Pb}/^{204}\text{Pb} \sim 15.5$ .

basanites,  $\lambda_0 = 3.56 \pm 0.07$ , is too high to have been produced by melting of primitive mantle (Palme and O'Neill, 2013). Aside from the REEs, the low  $\text{K/Nb}$  ratio ( $159 \pm 28$ ) relative to that of primitive mantle ( $\sim 400$ ) indicates that amphibole was also present in the source region (Witte et al., 2017). As amphibole breaks down above  $\sim 3$ – $3.5$  GPa and  $\sim 1150^\circ\text{C}$  for typical peridotite (Wallace and Green, 1991; Mandler and Grove, 2016), it could have existed only in the lithospheric mantle. It is noteworthy that the Sr-Nd-Pb isotope systematics of the Batain basanites (Witte et al., 2017; Nasir et al., 2006) share affinities with products of the Afar plume (Schilling et al., 1992; Pik et al., 1999; Furman et al., 2006) (Fig. 3b), which has been active since  $\sim 45$  Ma (Rooney, 2017). This shows that the Batain basanites likely represent mixtures of melts from a plume, with a source isotopically resembling a potential Afar plume component, and lithospheric derived sources.

Assuming mantle plumes are fixed, or moving very slowly relative to tectonic plates, a reconstruction of the past location of the basanites and underlying lithosphere to 40 Ma (Fig. 4) yields two crucial inferences: i) considered alongside the aforementioned geochemical diagnostics, the close proximity of the basanites paleo-positions at the time of their eruption to the location of the Afar plume indicates that these alkaline rocks are likely a product of the Afar plume. Most of the present offset is due to Arabian plate motion; only a moderate conduit tilt, consistent with global hotspot statistics (e.g., Steinberger et al., 2004), is required. The location of these basanites above the present-day Dani plume is thus to be taken as coincidental; and ii) the onset of basanite eruptions to the surface at  $\sim 35$ – $40$  Ma coincides with the passage of less than 100 km-thick lithosphere, at least 60 km thinner than the average Arabian lid (Fig. 4), above the Afar plume, facilitating decompression melting (Davies, 1994). We emphasize that any surface evidence of the Dani plume up until  $\sim 7$  Ma has been lost via subduction of the Tethys Ocean beneath Eurasia and associated continental collision (Fig. 4).

### 3.3. Topographic expression of the Dani plume through time

Despite experiencing minimal tectonic shortening since the Paleogene (66–23 Ma), Paleocene-Early Eocene ( $\sim 66$ – $41$  Ma) shallow-marine sediments of the Salma Plateau, which overlie the Dani plume, are currently found at elevations exceeding 2000 meters (Pavlopoulos et al., 2023). Furthermore, ongoing uplift is evidenced by elevated Quaternary

(2.58 Ma – present-day) marine terraces (Pavlopoulos et al., 2023; Hoffmann et al., 2020). The current uplift rate is modest, measuring less than 1 mm/yr, and fades towards the northwest along eastern Oman's coastline, as a function of distance from the imaged plume center (Hoffmann et al., 2020).

Receiver-function analyses (Weidle et al., 2022) indicate that the Salma plateau in eastern Oman lacks substantially thickened crust (mean thickness of  $\sim 34$  km), indicating that regional topography is not isostatically supported by a buoyant crustal root. The alternative is that this uplift is driven by upwelling mantle flow, via so-called dynamic topography (Wang and Li, 2021; Davies et al., 2023). An estimate of present-day residual topography (Holdt et al., 2022) (i.e., following removal of all known isostatic contributions) is illustrated in Fig. 5, in which we adopt up to a maximum spherical harmonic degree of  $l=30$  to focus on longer wavelength structures and limit the impact of flexural processes (e.g., a possible forebulge from Makran subduction). A positive residual topography is visible in the region overlying the Dani plume. Given that eastern Oman is close to a long-lived subduction system, one would expect this region to be associated with a long-wavelength residual topography low (Rubey et al., 2017). The presence of a localized residual topography high, which is clearly distinct from that of the Afar plume, alongside geological observations of ongoing uplift, therefore supports the notion of mantle upwelling in this region that remains active at present day.

### 3.4. Dani plume deflects Indian plate motion

To further constrain the sub-lithospheric activity of the Dani plume, we turn to plate kinematics, which are sensitive to changes in the tectonic force balance – including changes possibly induced by plume activity. Increased sub-lithospheric viscous flow associated with the activity of the Dani plume would have increased shear stresses acting at the base of the vast Eurasian and African plates (Arabia separated from Africa at  $\sim 25$  Ma), as well as the smaller Indian plate. The motion of the latter plate is more likely to be affected by such changes in flow chiefly for two reasons: i) as the Dani plume lies northwest of the Indian plate at 40 Ma, its sub-lithospheric flow exerts stresses onto its base that are consistently oriented towards the southeast; ii) as the Indian plate's basal area is smaller than those of the Africa and Eurasian plates, the

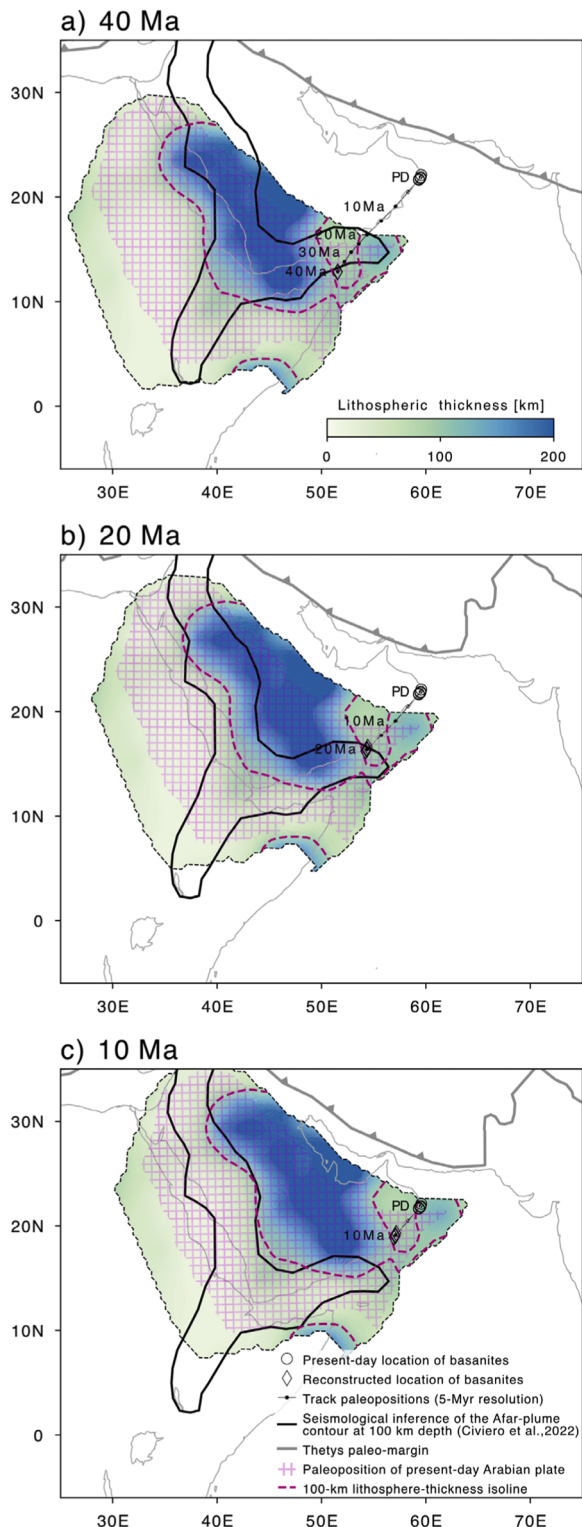


**Fig. 4. Paleo-position of Batain basanites.** a), b) and c) show the paleo-position of Arabian lithosphere and Batain basanites at 40 (age of oldest basanite eruption), 20 and 10 Ma, respectively. Present-day lithospheric thickness estimate (Davies et al., 2019) is colored and with a dashed-black contour. Regions to the north-east of the Arabian lithosphere are now subducted following closure of the Tethyan Ocean. Black outline of the Afar plume is from Civiero et al. (2022). Lithospheric thinning between Africa and Arabia started at ~25 Ma.

sum of Couette-type stresses at the lithosphere/asthenosphere interface that resist any change of plate motion is smaller for India, and thus possibly more prone to be overcome by the Poiseuille-type flow associated with asthenospheric plume flux. Thus, finding evidence of the arrival/strengthening of the Dani plume requires first interrogating kinematic reconstructions of Indian plate motion – although contemplating an impact also onto the African and/or Eurasian kinematics is not implausible.

Observations of ocean-floor magnetic reversals and fracture zones flanking the Carlsberg and northern Central Indian ridges (DeMets and Merkouriev, 2021) yield finite rotations that permit reconstructing the Cenozoic position of the Indian plate (IN) relative to the Somalia plate (SO) at high temporal resolution (~1 Myr). We input these to the REDBACK software (Iaffaldano et al., 2012, 2014), which implements a transdimensional hierarchical Bayesian framework in order to output noise-mitigated Euler vectors, in the specific case describing the motion of India in a reference frame fixed with Somalia. India/Somalia Euler vectors are used to calculate surface velocities at the indicated locations. REDBACK input parameters and output files (including noise-mitigated Euler vectors), as well as diagnostic reports are provided in Fig. S6. The past position of the Arabian lithosphere and the location of basanites found at present day are reconstructed relative to a fixed deep-mantle reference frame using the finite rotations of Africa relative to the Atlantic Hotspots system, and Arabia relative to Africa as reported in the Earthbyte repository (see earthbyte.org for more details and references). Since the finite rotations are reported without uncertainties in the form of covariance matrices, we elect to assign to each a diagonal covariance matrix whose entries are equal to 5% of the rotation angle. REDBACK allows us to obtain: i) noise-mitigated IN/SO Euler vectors; and ii) the probability of IN/SO kinematic changes through time. As the SO moves extremely slowly relative to the IN, the inferred plate-motion changes effectively mirror shifts of IN absolute motion. An expected probability peak of angular-velocity changes occurs around the time of the collision of the IN with Eurasia (EU) (Fig. 6a). However, a previously-undetected feature arising from these analyses is the non-negligible probability of changes of the IN Euler pole – which determines chiefly the direction of IN motion – between ~40 and ~20 Ma (Fig. 6a). The emerging pattern (Fig. 6b) is one where, until long after the collision-related slowdown of IN/EU convergence, the IN motion becomes slowly but steadily more eastward-oriented. Such a pattern cannot result from continental collision, because the impact of the latter onto the Indian motion occurred within a narrow period of ~5 Myr (Fig. 6b).

We hypothesize that the deflection of the Indian plate results from the Dani-plume activity and the associated asthenospheric radial flow-pattern (Fig. 6c), whose component underneath the IN is directed south-eastwards and might thus change its motion direction. Thus, we calculate torque-variations required upon India in order to change its Euler vector as evidenced by the kinematic reconstruction following the method reported in Iaffaldano and Bunge (2015) (see equations therein for more details). Such a method builds on differentiating the torque-balance equation at two relatively close geological instants, resulting in an equation where only torques that have actually changed within the time interval at hand remain linked to Euler-vector changes over the same time interval. In order to calculate the torque-variation imparted to India by establishment/strengthening of plume-flux we follow the method used by Iaffaldano et al. (2018). Plume-flux torque-variations are calculated as the integral of Poiseuille-type shear stresses over the basal area of the plate at hand (India in this case). The latter stresses are inferred analytically from conservation of the plume material, after having assumed the diameter of the plume conduit, and up-conduit plume-flux variation. The up-conduit plume-flux variation is kept as a free parameter of the problem, while we set the diameter of the Dani plume-conduit equal to 300 km – consistent with tomographic inferences reported in this study. Both torque-variation calculations require an assumption about the average viscosity of Earth's asthenosphere, its thickness, and a contour of the tectonic plate at hand. Here we

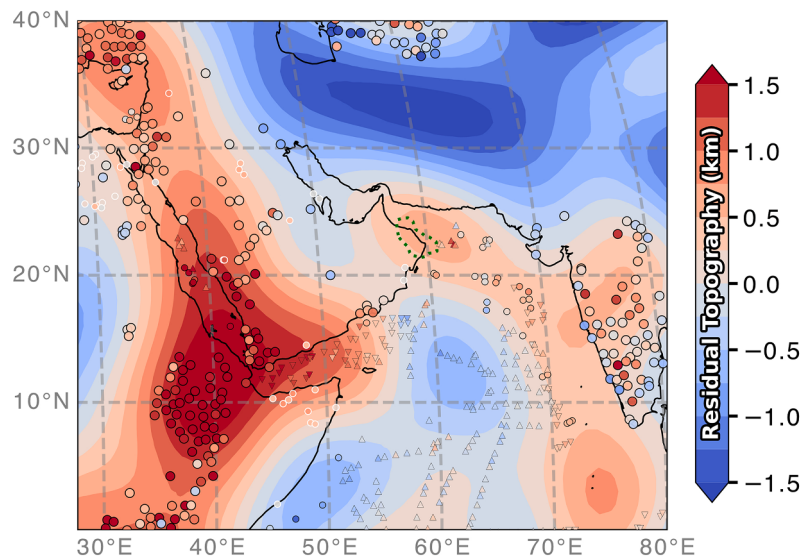


**Fig. 5. Positive present-day residual topography above Dani plume.** Spherical harmonic representation of present-day residual topography, up to a maximum spherical harmonic degree of  $l=30$ . In the oceanic realm, circles = measurements with both sediment and crustal thickness corrections; downward/upward-pointing triangles = measurements that are upper/lower limits with only sedimentary corrections. In the continental realm, large circles with black edges = measurements obtained by analysis of receiver functions, by controlled source seismic wide-angle and by vintage refraction experiments; smaller circles with white edges = elevations of onshore marine strata. Green dashed line is the location of the Dani plume inferred from the tomographic models.

set the global average of Earth's asthenosphere viscosity equal to  $10^{19}$  Pa s. Instead, the asthenosphere thickness is derived by implementing the constraint from modelling long-wavelength glacial rebound data, which indicates that the cube of asthenosphere viscosity is proportional to the viscosity contrast between asthenosphere and upper mantle. Here we assume a viscosity of the upper mantle equal to  $1.5 \times 10^{21}$  Pa s.

We compare two torque variations: the first is the torque variation required upon the IN plate to change its Euler vector from that reconstructed for the stage 46.235-to-43.450 Ma to that for stage 33.214-to-29.183 Ma (Fig. 6c). The second is the torque variation provided to the IN plate by the change in Dani-plume flow-pattern (Fig. 6c). By comparison, we also estimate the torque-variations provided by a hypothesized strengthening of Afar-plume flow. We find the former estimate best fits that required to deflect the IN motion between  $\sim 40$  and  $\sim 20$  Ma. Next, we interrogate in a similar fashion the African/North America kinematic record, which is available for the Cenozoic (Müller et al., 1999), although it features admittedly lower temporal resolution that does not warrant noise mitigation. We find that also the African plate motion changed direction between  $\sim 40$  and  $\sim 20$  Ma relative to North America. While in this case we cannot ascribe the absolute plate-motion change with high confidence to either plate, we note that if the change concerned mostly or entirely the African plate, it would be consistent with the hypothesized arrival/strengthening of the Dani plume. A torque-variation analysis identical to that performed for the Indian plate confirms the geodynamical plausibility of the impact of the Dani plume activity onto the kinematics of nearby plates (Fig. S7).

#### 4. Discussion and conclusions

In the presence of a positive thermal anomaly, the d410 phase transition from olivine to wadsleyite deepens due to a positive Clapeyron slope, indicating that it requires higher pressure and depth. Conversely, the d660 phase transition from ringwoodite to perovskite and magnesiowüstite shallows because of a negative Clapeyron slope, which implies a requirement for lower pressure and depth. Using the maximum observed perturbations of the d410 and d660 from the profiles shown in Fig. 1, we estimated the temperature anomaly required to generate such changes based on Clapeyron slope values. For the d410, maximum and minimum Clapeyron slopes of 4 MPa/K and 1.8 MPa/K

correspond to excess temperature anomalies of 105 K and 233 K for a depression of 14 km. Similarly, for the d660, slopes of -4 MPa/K and -2 MPa/K yield temperature anomalies of 150 K and 300 K for a 20 km elevation. These estimates are consistent with the temperature values inferred from our tomographic model. However, we note that the velocity model used for time-to-depth conversion of the receiver function (see Fig. S8), as well as the exclusion of compositional effect on the perturbation of the discontinuity depths (i.e., temperature-induced changes alone are assumed), may influence the inferred temperature estimates. We argue that the observed negative and positive deflections of the d410 and d660 discontinuities, respectively, suggest a positive thermal anomaly beneath eastern Oman, which extends throughout the upper mantle and supports tomographic imaging evidence indicating the presence of the Dani plume.

Given that the resolving power of our imaging is limited to a depth of 600–700 km (a constraint imposed by the aperture of our seismic network), we must rely on global tomographic models to investigate the potential roots of the Dani plume. Seismic imaging of the lower third of the mantle has traditionally been hampered by poor resolution, resulting from limited data sampling, the intrinsic attenuation of seismic waves with depth, and the broader sensitivity kernels at these depths. A recent tomographic model, DETOX-P3 (Hosseini et al., 2020), improves upon these limitations by incorporating many multifrequency measurements of core-diffracted P arrival times (Pdiff), along with P and PP arrival times, thereby significantly enhancing spatial resolution throughout the mantle. We extract two vertical profiles from the tomographic model DETOX-P3, extending from the surface down to the CMB, as shown in Fig. 7. Profile A, although with a lower resolution than our tomographic model (Fig. 1), confirms that a slow velocity anomaly is present beneath north-eastern Oman. Furthermore, it suggests that the Dani plume extends to at least 1200 km in depth before deflecting southwestward, where it appears to connect with a low-velocity conduit at the CMB – the same conduit feeding the Afar plume further to the southwest, in a tree-like structure akin to the Indo-African plume (Tsekhnistrenko et al., 2021).

This study presents interdisciplinary evidence for the existence of a “ghost” plume beneath eastern Oman – the Dani plume. The data afforded by our dense seismic deployment allow us to detect what is likely the thermal upper-mantle expression of a plume originating from

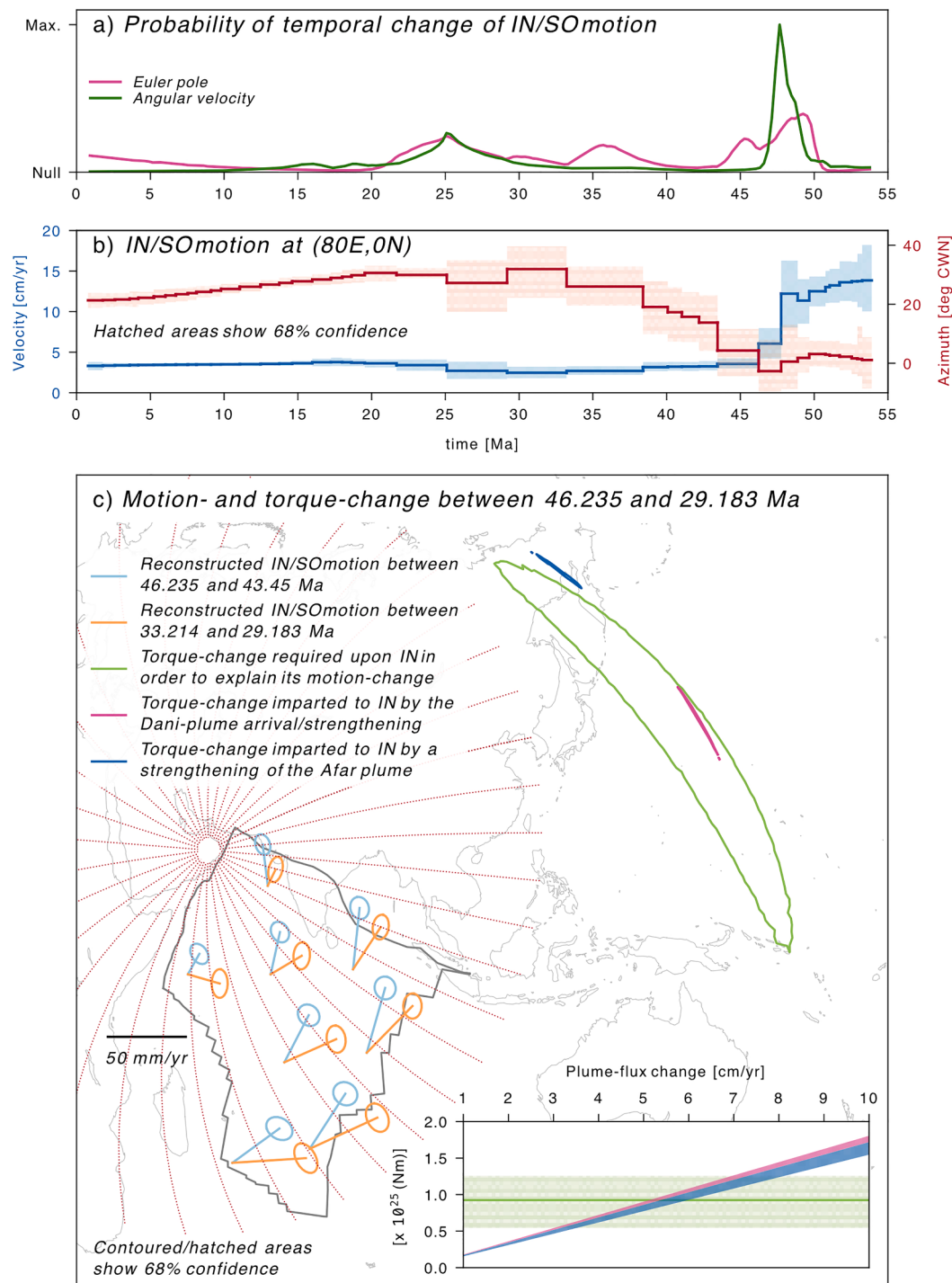


**Fig. 6. Motion and dynamics of Indian plate.** a) Probability of temporal change in angular velocity and Euler pole of the IN/SO motion. b) Motion and azimuth of IN calculated at (80E, 0N). c) Main panel shows changes of motion (in blue and orange) of the IN (in black its contour at ~45 Ma) between ~46 and ~29 Ma, and torque-variation pole (68% confidence area) required to explain the IN plate-motion change (in green) as well as associated with the Dani and Afar plumes (dotted red lines show radial flow propagating from the former one). Inset shows the associated torque-variation magnitudes, which in the case of plumes are estimated as a function of the assumed plume-conduit flux-change (Iaffaldano et al., 2018). The contour of the Indian plate through time is taken from the Earthbyte plate shapefiles (see earthbyte.org for more details).

the same reservoir that feeds Afar. We provide evidence from seismic tomography, topography of the d410 and d660 seismic discontinuities, present-day residual topography, the geological and geochemical record, kinematic reconstructions, and torque-variation calculations. While individual results alone may appear inconclusive, their collective contribution provides a consistent and robust interpretation. Our results, however, raise a further question, that has global consequences: *is the*

*Dani plume unique, or do similar ghost plumes exist elsewhere on Earth?* A potential present-day example is the continuous low-velocity conduit that extends from the lithosphere to the CMB beneath the Coral Sea (French and Romanowicz, 2015): this conduit lacks surface volcanic activity, but its presence has been confirmed using diverse observational constraints (Kennett and Davies, 2020). The African continent, where thick lithosphere restricts decompression melting associated with

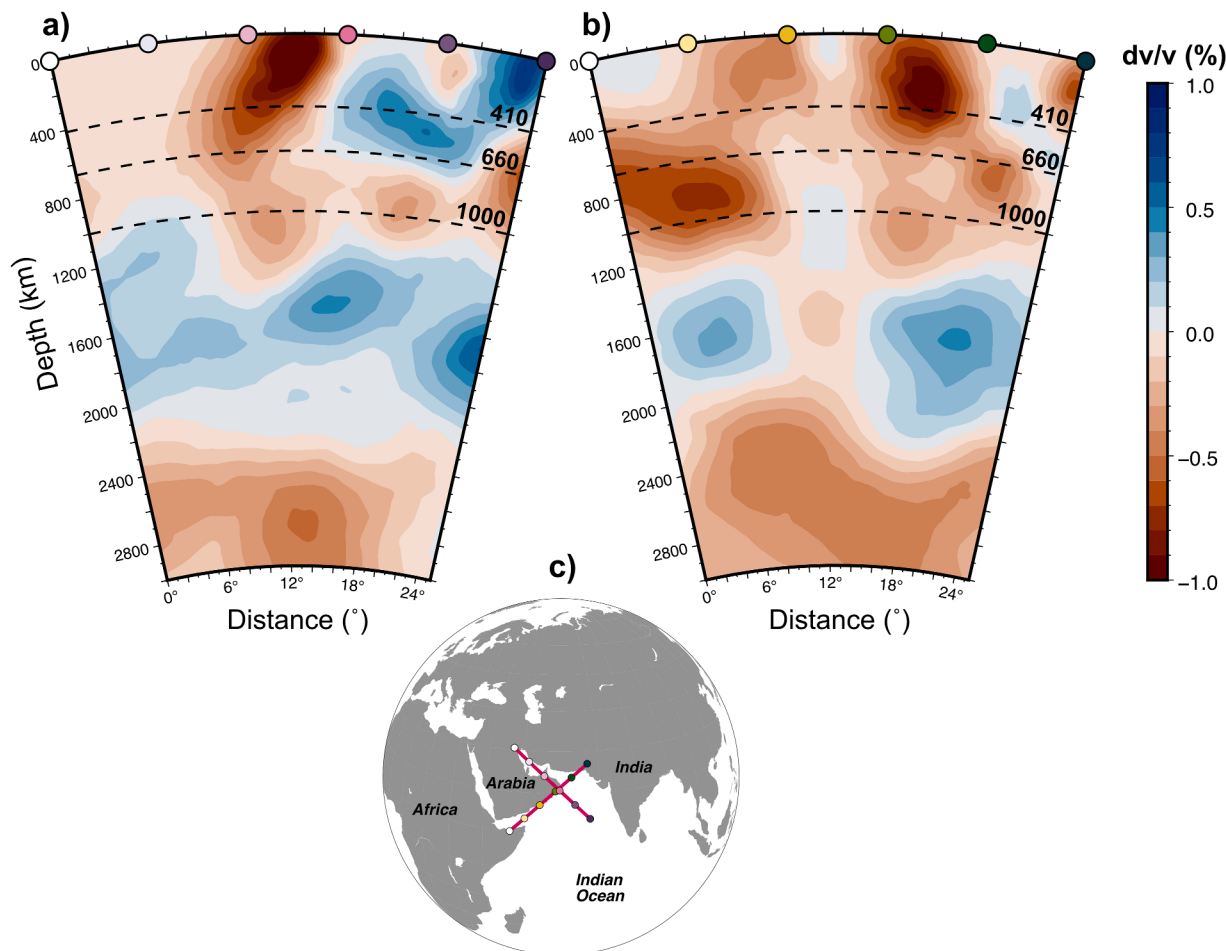


**Fig. 7. Tomographic images of the Dani plume from DETOX-P3.** (a, b) Vertical profiles extracted from the global tomographic model DETOX-P3. Coloured dots on top of each profile are for aiding location of the profiles as illustrated in panel c).

plumes rising from the deep-mantle African Large-Low-Velocity-Province, is also a prime candidate location: in addition to the continental magmatic hotspots of Afar, Hoggar, and Tibesti, several prominent anorogenic and amagmatic swells have been identified (Hoggard et al., 2020). Finally, in older parts of the Pacific Ocean, underlain by cooler and thicker oceanic lithosphere, there is evidence for topographic swells with wavelengths of  $\sim 1000$  km that are not associated with known mantle plumes. When considered alongside strong evidence for ghost plumes in the geological record, for example, beneath both the North American (Chu et al., 2013) and Australian continents (Davies et al., 2015), it is likely that the geoscientific community is only beginning to scratch the surface. Our findings prompt a reconsideration of the heat flux transported by plumes. Considering that the volume of magmatic swells is half of the same amagmatic features invokes a significant increase in estimates for the heat flux across the CMB (Lay et al., 2008). An augmented CMB heat flux bears implication for thermal evolution models of our planet, and potential revisions to account for the distribution of heat-producing elements, including those sequestered in the lower mantle and in the core (Lay et al., 2008).

## Contributions

S.P. conceived this study and integrated all observational constraints. S.P., D.R.D. and G.I. made the main interpretation. H.H., S.P. and D.Z. created the tomographic models. M.I. and S.P. estimated the depth of mantle discontinuities using receiver-function analysis. G.I. analysed kinematic reconstructions and performed calculations of torque variations. P.S. and S.W. analysed the geochemical data. S.P. wrote

the paper, following discussion with, and contributions from, all authors.

Correspondence can also be sent to simone.pilia@kfupm.edu.sa.

## Open research

The COOL passive seismic dataset from Oman is accessible through the IRIS Data Management (see [https://www.fdsn.org/networks/detail/5H\\_2013/](https://www.fdsn.org/networks/detail/5H_2013/)). The seismic dataset for the UAE stations is from Pilia et al. (2020a). Data from 30 stations of the national seismic networks in the UAE, Oman and Bahrain are restricted but may be obtained by contacting the respective seismological centres.

REDBACK is released open source under the GNU General Public License and can be obtained at <http://www.iearth.edu.au/codes/REDBACK/>. The tomographic software used in this study can be obtained from D. Zhao (zhao@tohoku.ac.jp) upon request.

## Declaration of competing interest

The authors declare that they have no known competing financial interests or personal relationships that could have appeared to influence the work reported in this paper.

## Acknowledgments

S.P. would like to acknowledge the support provided by the Deanship of Research Oversight and Coordination (DROC) at King Fahd University of Petroleum and Minerals (KFUPM) for funding this work through

project No. EC231003. S.W. acknowledges support from KFUPM grant CPG 21107. H.H. acknowledges support from the National Natural Science Foundation of China (grant 42106068) and the China Postdoctoral Science Foundation (grant 2021M691412). D.Z. acknowledges support from Japan Society for the Promotion of Science (JSPS) grant 19H01996.

We thank Bernhard Steinberger and Mingming Li for their constructive reviews.

## Supplementary materials

Supplementary material associated with this article can be found, in the online version, at [doi:10.1016/j.epsl.2025.119467](https://doi.org/10.1016/j.epsl.2025.119467).

## Data availability

Data will be made available on request.

## References

- Baker, J.A., Menzies, M.A., Thirlwall, M.F., Macpherson, C.G., 1997. Petrogenesis of Quaternary intraplate volcanism, Sana'a, Yemen: implications for plume-lithosphere interaction and polybaric melt hybridization. *J. Petrol.* 38, 1359–1390.
- Brocher, T.M., 2005. Empirical relations between elastic wavespeeds and density in the Earth's crust. *Bull. Seism. Soc. Am.* 95, 2081–2092.
- Chu, R., Leng, W., Helmberger, D.V., Gurnis, M., 2013. Hidden hotspot track beneath the eastern United States. *Nat. Geosci.* 6, 963–966.
- Civiero, C., Lebedev, S., Celli, N., 2022. A complex mantle plume head below East Africa–Arabia shaped by the lithosphere–asthenosphere boundary topography. *Geochem., Geophys., Geosyst.* 23, e2022GC010610.
- Courtillot, V., Davaille, A., Besse, J., Stock, J., 2003. Three distinct types of hotspots in the Earth's mantle. *Earth, Planet, Sci. Lett.* 205, 295–308.
- Dasgupta, R., Hirschmann, M.M., 2010. The deep carbon cycle and melting in Earth's interior. *Earth, Planet, Sci. Lett.* 298, 1–13.
- Davies, G.F., 1994. Thermomechanical erosion of the lithosphere by mantle plumes. *J. Geophys. Res.* 99, 15709–15722.
- Davies, D.R., Rawlinson, N., Iaffaldano, G., Campbell, I., 2015. Lithospheric controls on magma composition along Earth's longest continental hotspot track. *Nature* 525, 511–514.
- Davies, D.R., Valentine, A.P., Kramer, S.C., Rawlinson, N., Hoggard, M.J., Eakin, C.M., Wilson, C.R., 2019. Earth's multi-scale topographic response to global mantle flow. *Nat. Geosci.* 12, 845–850.
- Davies, D.R., Ghelichkhan, S., Hoggard, M.J., Valentine, A.P., Richards, F.D., 2023. Observations and models of dynamic topography: Current status and future directions. *Dyn. Plate Tecton. Mantle Convect.* 223–269.
- DeMets, C., Merkuriev, S., 2021. Detailed reconstructions of India–Somalia Plate motion, 60 Ma to present: implications for Somalian Plate absolute motion and India–Eurasia Plate motion. *Geophys. J. Int.* 227, 1730–1767.
- Dongmo Wamba, M., Montagner, J., Romanowicz, B., 2023. Imaging deep-mantle plumbing beneath La Réunion and Comores hot spots: Vertical plume conduits and horizontal ponding zones. *Sci. Adv.* 9.
- French, S., Romanowicz, B., 2015. Broad plumes rooted at the base of the Earth's mantle beneath major hotspots. *Nature* 525.
- Furman, T., et al., 2006. Heads and tails: 30 million years of the Afar plume. *Geol. Soc. Spec. Publ.* 259, 95–119.
- Gerya, T.V., Stern, R.J., Baes, M., Sobolev, S.V., Whattam, S.A., 2015. Plate tectonics on the Earth triggered by plume-induced subduction initiation. *Nature* 527, 221–225.
- Goes, S., Govers, R., Vacher, A.P., 2000. Shallow mantle temperatures under Europe from P and S wave tomography. *J. Geophys. Res. Solid. Earth.* 105, 11153–11169.
- Goes, S., Cammarano, F., Hansen, U., 2004. Synthetic seismic signature of thermal mantle plumes. *Earth, Planet, Sci. Lett.* 218, 403–419.
- Hill, R.I., 1991. Starting plumes and continental break-up. *Earth, Planet, Sci. Lett.* 104, 398–416.
- Hirschmann, M.M., 2000. Mantle solidus: Experimental constraints and the effects of peridotite composition. *Geochem., Geophys., Geosyst.* 1.
- Hoffmann, G., et al., 2020. Quaternary uplift along a passive continental margin (Oman, Indian Ocean). *Geomorphology* 350, 106870.
- Humphreys, E.R., Niu, Y., 2009. On the composition of ocean island basalts (OIB): The effects of lithospheric thickness variation and mantle metasomatism. *Lithos* 112, 118–136.
- Hoggard, M.J., Parnell-Turner, R., White, N., 2020. Hotspots and mantle plumes revisited: Towards reconciling the mantle heat transfer discrepancy. *Earth, Planet, Sci. Lett.* 542, 116317.
- Holdt, M., White, N., Stephenson, S., Conway-Jones, B., 2022. Densely sampled global dynamic topographic observations and their significance. *J. Geophys. Res. Solid. Earth.* 127.
- Hosseini, K., Sigloch, K., Tsekhnistrenko, M., Zaheri, A., Nissen-Meyer, T., Igel, H., 2020. Global mantle structure from multifrequency tomography using P, PP and P-diffracted waves. *Geophys. J. Int.* 220, 96–141.
- Hu, H., Zhao, D., Lin, J., Pilia, S., 2023. A Slab Window Beneath North Sumatra Revealed by P-Wave Mantle Tomography. *J. Geophys. Res. Solid. Earth.* 128, e2022JB025976.
- Iaffaldano, G., Bodin, T., Sambridge, M., 2012. Reconstructing plate-motion changes in the presence of finite-rotations noise. *Nat. Commun.* 3, 1048–1059.
- Iaffaldano, G., Hawkins, R., Bodin, T., Sambridge, M., 2014. REDBACK: Open-source software for efficient noise-reduction in plate kinematic reconstructions. *Geochem., Geophys., Geosyst.* 15, 1663–1670.
- Iaffaldano, G., Bunge, H., 2015. Rapid plate motion variations through geological time: Observations serving geodynamic interpretation. *Annu Rev. Earth. Planet. Sci.* 43, 571–592.
- Iaffaldano, G., Davies, D.R., DeMets, C., 2018. Indian Ocean floor deformation induced by the Reunion plume rather than the Tibetan Plateau. *Nat. Geosci.* 11, 362–366.
- Ismaiel, M., et al., 2023. Moho topography and crustal properties in the UAE and northern Oman mountain belt from teleseismic receiver functions. *Geophys. J. Int.* 233, 2084–2100.
- Ito, E., Takahashi, E., 1989. Postspinel transformations in the system  $Mg_2SiO_4$ – $Fe_2SiO_4$  and some geophysical implications. *J. Geophys. Res.* 94, 10637–10646.
- Katsura, T., Ito, E., 1989. The system  $Mg_2SiO_4$ – $Fe_2SiO_4$  at high pressures and temperatures: Precise determination of stabilities of olivine, modified spinel, and spinel. *J. Geophys. Res.* 94, 15663–15670.
- Katz, R.F., Spiegelman, M., Langmuir, C.H., 2003. A new parameterization of hydrous mantle melting. *Geochem., Geophys., Geosyst.* 4.
- Kennett, B., Engdahl, E., Buland, R., 1995. Constraints on seismic velocities in the Earth from traveltimes. *Geophys. J. Int.* 122, 108–124.
- Kennett, B.L.N., Davies, D.R., 2020. Intra-plate volcanism in North Queensland and eastern new Guinea: A cryptic mantle plume? *Gondwana Res.* 79, 209–216.
- Koppers, A., et al., 2021. Mantle plumes and their role in Earth processes. *Nat. Rev. Earth Environ.* 2, 382–401.
- Lay, T., Hernlund, J., Buffett, B.A., 2008. Core–mantle boundary heat flow. *Nat. Geosci.* 1, 25–32.
- Lee, C., et al., 2009. Constraints on the depths and temperatures of basaltic magma generation on Earth and other terrestrial planets using new thermobarometers for mafic magmas. *Earth, Planet, Sci. Lett.* 279, 20–33.
- Ligorria, J.P., Ammon, C.J., 1999. Iterative deconvolution and receiver-function estimation. *Bull. Seism. Soc. Am.* 89, 1395–1400.
- Mandler, B., Grove, T., 2016. Controls on the stability and composition of amphibole in the Earth's mantle. *Contrib. Mineral. Petrol.* 171, 1–20.
- Morgan, W., 1971. Convection Plumes in the Lower Mantle. *Nature* 230, 42–43.
- Müller, R.D., Royer, J.Y., Cande, S.C., Roest, W.R., Maschenkov, S., 1999. New constraints on the Late Cretaceous/Tertiary plate tectonic evolution of the Caribbean. *Sedimentary Basins of the World* 4, 33–59.
- Müller, R.D., et al., 2019. A global plate model including lithospheric deformation along major rifts and orogens since the Triassic. *Tectonics*. 38.
- Nasir, S., Al-Sayigh, A., Alharthy, A., Al-Lazki, A., 2006. Geochemistry and petrology of Tertiary volcanic rocks and related ultramafic xenoliths from the central and eastern Oman Mountains. *Lithos* 90, 249–270.
- O'Neill, H.S.C., 2016. The smoothness and shapes of chondrite-normalized rare earth element patterns in basalts. *J. Petrol.* 57, 463–1508.
- Palme, H., O'Neill, H.S.T.C., 2013. Cosmochemical estimates of mantle composition: The mantle and core. Elsevier, pp. 1–39.
- Pavlopoulos, K., et al., 2023. Uplift dynamics of the obducted northeastern continental margin of the Arabian Peninsula, Sultanate of Oman. *Geochem., Geophys., Geosyst.* 24, 2023GC011054.
- Pik, R., Deniel, C., Coulon, C., Yirgu, G., Marty, B., 1999. Isotopic and trace element signatures of Ethiopian flood basalts: evidence for plume–lithosphere interactions. *Geoch. et Cosmoch. Acta* 63, 2263–2279.
- Pilia, S., Jackson, J.A., Hawkins, R., Kaviani, A., Ali, M.Y., 2020a. The southern Zagros collisional orogen: new insights from transdimensional trees inversion of seismic noise. *Geophys. Res. Lett.* 47, e2019GL086258.
- Pilia, S., Hu, H., Ali, M.Y., Rawlinson, N., Ruan, A., 2020b. Upper mantle structure of the northeastern Arabian Platform from teleseismic body-wave tomography. *Phys. Earth Planet. Inter.* 307, 106549.
- Pilia, S., Davies, D.R., Hall, R., Bacon, C.A., Gilligan, A., Greenfield, T., Tongkul, F., Kramer, S.C., Wilson, C.R., Ghelichkhan, S., Cornwell, D.G., 2023. Post-subduction tectonics induced by extension from a lithospheric drip. *Nat. Geosci.* 16, 646–652.
- Plank, T., Forsyth, D.W., 2016. Thermal structure and melting conditions in the mantle beneath the Basin and Range province from seismology and petrology. *Geochem., Geophys., Geosyst.* 17, 1312–1338.
- Rawlinson, N., Kennett, B., 2004. Rapid estimation of relative and absolute delay times across a network by adaptive stacking. *Geophys. J. Int.* 157, 332–340.
- Rooney, T.O., 2017. The Cenozoic magmatism of East-Africa: Part I—Flood basalts and pulsed magmatism. *Lithos* 286, 264–301.
- Rubey, M., et al., 2017. Global patterns in Earth's dynamic topography since the Jurassic: the role of subducted slabs. *Solid Earth* 8, 899–919.
- Schilling, J., Kingsley, R., Hanan, B., McCully, B., 1992. Nd-Sr-Pb isotopic variations along the Gulf of Aden: Evidence for Afar mantle plume–continental lithosphere interaction. *J. Geophys. Res. Solid. Earth.* 97, 10927–10966.
- Sobolev, S.V., et al., 2011. Linking mantle plumes, large igneous provinces and environmental catastrophes. *Nature* 477, 312–316.
- Stein, M., Hofmann, A.W., 1992. Fossil plume head beneath the Arabian lithosphere? *Earth, Planet, Sci. Lett.* 114, 193–209.
- Steinberger, B., Sutherland, R., O'Connell, R.J., 2004. Prediction of Emperor-Hawaii seamount locations from a revised model of global plate motion and mantle flow. *Nature* 430, 167–173.
- Steinberger, B., Becker, T.W., 2018. A comparison of lithospheric thickness models. *Tectonophysics*. 746, 325–338.

- Stixrude, L., Lithgow-Bertelloni, C., 2012. Geophysics of chemical heterogeneity in the mantle. *Annu. Rev. Earth. Planet. Sci.* 40, 569–595.
- Styles, E., Goes, S., van Keken, P.E., Ritsema, J., Smith, H., 2011. Synthetic images of dynamically predicted plumes and comparison with a global tomographic model. *Earth. Planet. Sci. Lett.* 311, 351–363.
- Torsvik, T.H., Burke, K., Steinberger, B., Webb, S.J., Ashwal, L.D., 2010. Diamonds sampled by plumes from the core–mantle boundary. *Nature* 466, 352–355.
- Tsekhnistrenko, M., Sigloch, K., Hosseini, K., Barruol, G., 2021. A tree of Indo-African mantle plumes imaged by seismic tomography. *Nat. Geosci.* 14, 612–619.
- Wallace, M., Green, D.H., 1991. The effect of bulk rock composition on the stability of amphibole in the upper mantle: implication for solidus positions and mantle metasomatism. *Mineral. Petrol.* 44, 1–19.
- Walter, M.J., Cottrell, E., 2024. Equilibrium constraints on partial melting in the upper mantle. In: Anbar, A., Weis, D. (Eds.), *Treatise on Geochemistry*, 3rd ed. Elsevier, B. V, pp. 231–273.
- Wang, Y., Li, M., 2021. The interaction between mantle plumes and lithosphere and its surface expressions: 3-D numerical modelling. *Geophys. J. Int.* 225, 906–925.
- Weidle, C., Agard, P., Meier, T., Ducassou, C., El-Hussain, I., 2013. COOL (Crust of the Oman Ophiolite and its Lithosphere) seismic network. *GEOFON Data Archive*. [https://doi.org/10.7914/SN/5H\\_2013](https://doi.org/10.7914/SN/5H_2013).
- Weidle, C., et al., 2022. A 3-D crustal shear wave velocity model and Moho map below the Semail Ophiolite, eastern Arabia. *Geophys. J. Int.* 231, 817–834.
- Witte, M., et al., 2017. OIB signatures in basin-related lithosphere-derived alkaline basalts from the Batain basin (Oman) - Constraints from  $^{40}\text{Ar}/^{39}\text{Ar}$  ages and Nd–Sr–Pb–Hf isotopes. *Lithos* 286, 109–124.
- Wolfe, C.J., Bjarnason, Th., VanDecar, I., Solomon, S., 1997. Seismic structure of the Iceland mantle plume. *Nature* 385, 245–247.
- Xu, M., He, J., 2023. Seispy: Python module for batch calculation and postprocessing of receiver functions. *Seismol. Soc. Am.* 94, 935–943.
- Zhao, D., Hasegawa, A., Kanamori, H., 1994. Deep structure of Japan subduction zone as derived from local, regional, and teleseismic events. *J. Geophys. Res.* 99, 22313–22329.